JOURNAL OF AIRCRAFT
Vol. 46, No. 3, May–June 2009

Detached-Eddy Simulations of Vortex Breakdown over a 70-Degree Delta Wing

Scott Morton*
U.S. Air Force Academy, Colorado Springs, Colorado 80840

DOI: 10.2514/1.4659

An understanding of the vortical structures that comprise the vortical flowfield around slender bodies is essential for the development of highly maneuverable and high angle-of-attack flight. This is primarily due to the physical limits this phenomenon imposes on aircraft and missiles at extreme flight conditions. Demands for more maneuverable air vehicles have pushed the limits of current computational fluid dynamics methods in the high Reynolds number regime. Simulation methods must be able to accurately describe the unsteady, vortical flowfields associated with fighter aircraft at Reynolds numbers more representative of full-scale vehicles. One of the goals of this paper is to demonstrate the ability of detached-eddy simulation, a hybrid Reynolds-averaged Navier–Stokes large-eddy simulation method, to accurately predict the vortical flowfield over a slender delta wing at Reynolds numbers above 1×10^6. Although detached-eddy simulation successfully predicted the location of the vortex breakdown phenomenon in previous work, the goal of the current effort is to further validate the method with additional experimental data from the Office National d'Etudes et Recherches Aérospatiales, such as surface pressures and turbulent kinetic energy in the vortex core. The effect of grid density and an adaptive mesh refinement technique is also assessed through comparisons with the experiment. Detailed wind-tunnel geometry, such as tunnel walls and the sting mount system, are simulated and found to make a measurable difference. Finally, modeling the laminar-to-turbulent transition is demonstrated to have a significant effect on the vortical flowfield.

Introduction

MANY of today's military vehicles exhibit vortex-dominated flowfields. At a recent NATO air vehicle technology conference, D. A. Lovell presented a review of "Military Vortices" [1], in which he discussed the declining research budget in this area and the importance of understanding the phenomenon. He classified vortex flows into three categories: "those designed into a vehicle to improve performance, those which cannot be avoided and whose adverse affects must be minimized, and those that were not expected to occur" [1]. He gives examples of many of these vortex-dominated flowfields: tip vortices on wings having low sweep, leading-edge extension vortices from the F-18 and F-16 aircraft, foreplanes on the Rafale, and flow over the MK-82 bomb, to name just a few. He also discusses the fact that governments are relying ever increasingly on the aerospace industry to perform research. Because the aerospace industry concentrates on cruise conditions for optimization of commercial aircraft, these vortical flowfields common in military aircraft are losing their place in research budgets. This is occurring at a time when the three largest U.S. fighter development programs (F/A-18E/F, F-22, and F-35) are incorporating twin tail configurations and high angle-of-attack maneuvering. The aerodynamic phenomenon causing concern for these twin tail aircraft is vortex breakdown, which can be modeled with the very simple flat plate delta wing geometry.

The delta wing vortex breakdown phenomenon has been studied extensively since Henri Werlé first photographed it in 1954 during water-tunnel tests of a slender delta wing model at the Office National d'Etudes et Recherches Aérospatiales (ONERA) [2]. This work was quickly confirmed by Peckham and Atkinson [3], Elle [4], and Lambourne and Bryer [5] and spawned a large number of experimental, computational, and theoretical studies that continue today. These investigations led to the development of several theories governing vortex breakdown, although none have been universally accepted [6–10]. Despite this lack of a unified theoretical interpretation, several forms of vortex breakdown have been identified [8,11] (i.e., bubble, helical, etc.), and the global characteristics of the phenomenon are understood. During the breakdown process, the mean axial velocity component rapidly decreases until it reaches a stagnation point and/or becomes negative on the vortex axis. This stagnation point, called the breakdown location, is unsteady and typically oscillates about some mean position along the axis of the vortex core [12,13]. As the angle of attack increases, the mean vortex breakdown location moves upstream over the delta wing (from the trailing edge toward the apex).

The primary vortex over a slender delta wing at angle of attack has been postulated to be principally inviscid. Unfortunately, the location of the vortex is strongly affected by a secondary vortex formed by the interrelationship between the surface boundary layer and the primary vortex. In addition, the vortex breakdown phenomenon creates turbulent kinetic energy that must be modeled properly or resolved. Many turbulence models create orders of magnitude at too high a level of turbulent eddy viscosity in the primary vortex core, which significantly alters the flowfield and in some cases eliminates breakdown observed experimentally at high Reynolds numbers. For these reasons, an accurate prediction of the flowfield over a slender delta wing at high angles of attack and high Reynolds numbers (as well as military aircraft exhibiting vortex breakdown) must model the boundary layer, primary and secondary vortex, and turbulent kinetic energy correctly.

Although advances have taken place in areas such as grid generation and fast algorithms for solutions of systems of equations, computational fluid dynamics (CFD) has remained limited as a reliable tool for prediction of inherently unsteady flows at flight Reynolds numbers. Current engineering approaches to the prediction of unsteady flows are based on the solution of the Reynolds-averaged Navier–Stokes (RANS) equations. The turbulence models employed in RANS methods necessarily model the entire spectrum of turbulent motions. Although often adequate in steady flows with no regions of reversed flow, or possibly exhibiting shallow separation, RANS turbulence models are inevitably unable to accurately predict flows characterized by massive separation. Unsteady, massively separated

---

Received 18 August 2003; revision received 4 April 2005; accepted for publication 10 December 2007.

*Professor, Department of Aeronautics, 2410 Faculty Drive; currently Director, Modeling and Simulation Research Center. Associate Fellow AIAA.

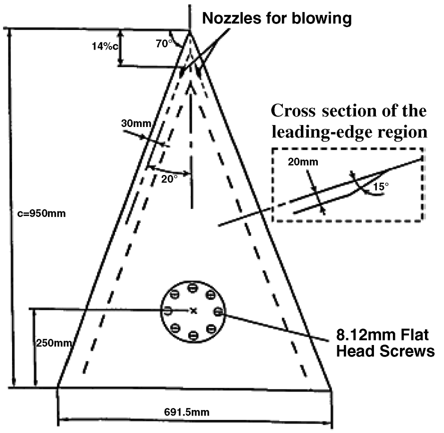

Fig. 1 Sketch of the delta wing model with nozzles for along-the-core blowing near the apex.

flows are characterized by geometry-dependent and three-dimensional turbulent eddies. These eddies, arguably, are what defeat RANS turbulence models of any complexity.

To overcome the deficiencies of RANS models for predicting massively separated flows, Spalart et al. [14] proposed a detached-eddy simulation (DES) with the objective of developing a numerically feasible and accurate approach combining the most favorable elements of RANS models and large-eddy simulations (LES). The primary advantage of DES is that it can be applied at high Reynolds numbers, as can Reynolds-averaged techniques, but it also resolves geometry dependent, unsteady, three-dimensional turbulent motions, as in LES. The unstructured finite volume solver *Cobalt* [15] has been used in conjunction with DES successfully for a number of complex problems, including a supersonic base flow [16], a delta wing vortex breakdown [17], a square with rounded corners [18], the F-15E at a high angle of attack [19], and the F/A-18E with an unsteady shock buffet [20].

A NATO working group from the Research and Technology Organization (AVT-080) has been tasked with assessing the ability of computational fluid dynamics to accurately predict vortex breakdown and to document the experimental database available for the verification and validation of CFD for delta wing vortex breakdown. The specific aim of this work is to document the ability of the hybrid RANS–LES method, DES, to accurately predict vortex breakdown position as well as the overall time evolution of this unsteady flowfield. In particular, grid refinement, wind-tunnel wall and sting effects, and laminar-to-turbulent transition will be analyzed for a 70 deg delta wing at $\alpha = 27$ deg, $M = 0.069$, and $Re_c = 1.56 \times 10^6$. Comparison of the computed results with the experiments of Mitchell et al. [13] will also be presented.

Experimental Method and Facilities

The experimental data used for comparison were obtained by Mitchell et al. [13] from ONERA's F2 wind tunnel. ONERA's F2 wind tunnel has a rectangular test section with a width of 1.4 m, a height of 1.8 m, and a length of 5 m. It is powered by a 680 kW dc motor that drives a fan with blades spanning 3.15 m and provides a maximum freestream velocity in the test section of 105 m/s. A cooling facility maintains a constant freestream temperature in the test section. The relative freestream velocity $\Delta U_0/U_0$ is estimated to have an accuracy of 1%, whereas the mean intensity of turbulence has an accuracy of 0.1% [13].

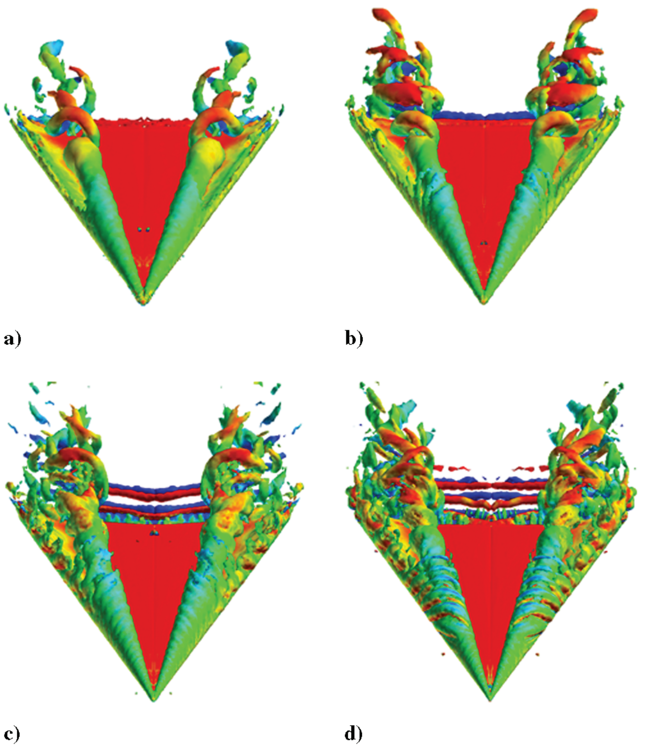

Fig. 2 Instantaneous isosurfaces of vorticity magnitude colored by the spanwise component of vorticity for four grids: a) G1 (1.2×10^6 cells), b) G2, (2.7×10^6 cells), c) G3 (6.7×10^6 cells), and d) G4 (10.7×10^6 cells). The flowfield conditions are $\alpha = 27$ deg, $M = 0.069$, and $Re_c = 1.56 \times 10^6$.

In the F2, the delta wing model depicted in Fig. 1 was mounted on a sting with a horizontal support and flexible joint for adjusting the angle of attack with an accuracy of ±0.05 deg. The horizontal support was manipulated in height along a vertical column so as to maintain the model close to the center axis of the test section. The model was mounted in the test section with no yaw angle with respect to the freestream flow (estimated accuracy of ±0.1 deg). The experimental data set consists of steady pressure data at many locations on the top side of the delta wing and laser Doppler velocimetry data in planes parallel to the top surface, perpendicular to the top surface spanwise, and perpendicular to the top surface along the vortex core.

Table 1 Unstructured grids developed for the ONERA 70 deg delta wing during the NATO Research and Technology Organization task group AVT-080

Name	Description	No. of cells	$X_{\min}$ to $X_{\max}$	$Y_{\min}$ to $Y_{\max}$	$Z_{\min}$ to $Z_{\max}$
G1	Half-span	1.2×10^6	$-10 < X < 10$ m	$0 < Y < 5$ m	$-5 < Z < 5$ m
G2	Half-span	2.7×10^6	$-10 < X < 10$ m	$0 < Y < 5$ m	$-5 < Z < 5$ m
G3	Half-span	6.7×10^6	$-10 < X < 10$ m	$0 < Y < 5$ m	$-5 < Z < 5$ m
G4	Half-span	10.7×10^6	$-10 < X < 10$ m	$0 < Y < 5$ m	$-5 < Z < 5$ m
G5	Half-span, walls	2.6×10^6	$-10 < X < 10$ m	$0 < Y < 2.5$ m	$-1.75 < Z < 1.75$ m
G6	Full span, walls, based on G5	5.2×10^6	$-10 < X < 10$ m	$-2.5 < Y < 2.5$ m	$-1.75 < Z < 1.75$ m
G7A1	Half-span, walls, sting	4.1×10^6	$-10 < X < 10$ m	$0 < Y < 2.5$ m	$-1.75 < Z < 1.75$ m
G8	Full span, walls, sting, based on G7	8.2×10^6	$-10 < X < 10$ m	$-2.5 < Y < 2.5$ m	$-1.75 < Z < 1.75$ m
G9	Half-span, no sting	1.2×10^6	$-10 < X < 10$ m	$0 < Y < 5$ m	$-5 < Z < 5$ m
G9A4	AMR of G9	2.4×10^6	$-10 < X < 10$ m	$0 < Y < 5$ m	$-5 < Z < 5$ m
G9A5	AMR of G9	2.5×10^6	$-10 < X < 10$ m	$0 < Y < 5$ m	$-5 < Z < 5$ m

Numerical Method

In this section, a brief description of the numerical method is provided with full details of the computational scheme and the solution method presented in [15]. Solutions were obtained for a freestream velocity of 24 m/s, an angle of attack of 27 deg, and a freestream pressure and temperature resulting in a Reynolds number of 1.56×10^6 and a freestream Mach number of 0.069. The numerical simulation matched the angle of attack, Reynolds number, and Mach number of the wind-tunnel experiments [13,21] previously described. Solutions are computed using the commercially available solver *Cobalt*. *Cobalt* is an unstructured finite volume method developed for solution of the compressible Navier–Stokes equations with details of the approach described in [15]. The method is cell centered and applicable to arbitrary cell topologies including hexahedrals, prisms, and tetrahedra. The spatial operator uses an exact Riemann solver, least-squares gradient calculations using QR Factorization to provide second-order accuracy in space, and total variation diminishing flux limiters to limit extrema at cell faces. A point implicit method using analytic first-order inviscid and viscous Jacobians is used for advancement of the discretized system. A Newton subiteration scheme is employed to improve time accuracy.

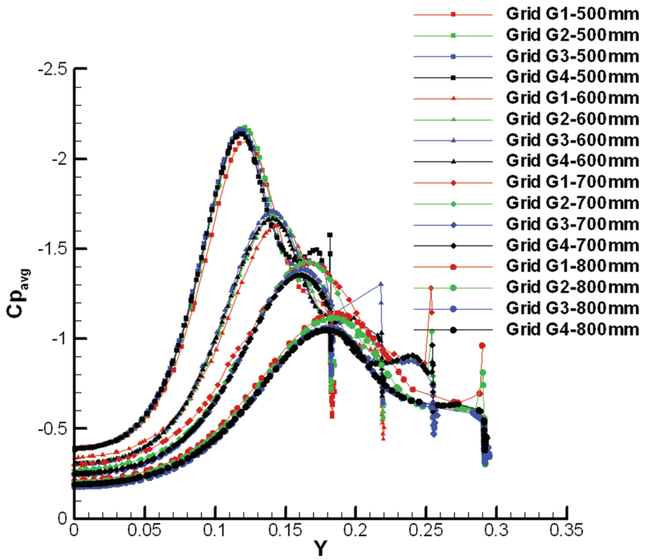

Fig. 3 Average surface pressure coefficients at four chordwise stations (500, 600, 700, and 800 mm) for grids G1, G2, G3, and G4.

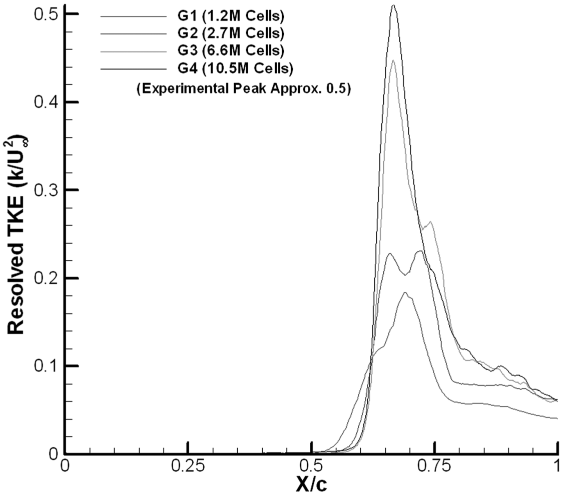

Fig. 4 Resolved turbulent kinetic energy nondimensionalized by the square of the freestream velocity along the core for four grids.

Table 2 Vortex breakdown positions for the experiments and various grids (vortex breakdown position is computed for many of the grids)

Grid	Mean	Variation
G1	0.50	±0.05
G2	0.58	±0.05
G3	0.62	±0.05
G4	0.62	±0.05
G5	0.67	±0.06
G6-left	0.7	±0.05
G6-right	0.71	±0.05
G7A1	0.605	±0.035
G9A5	0.61	±0.05
G7A1-SS	0.50	±0.02
G9A5-SS	0.63	±0.20
Experiment	0.65	±0.05

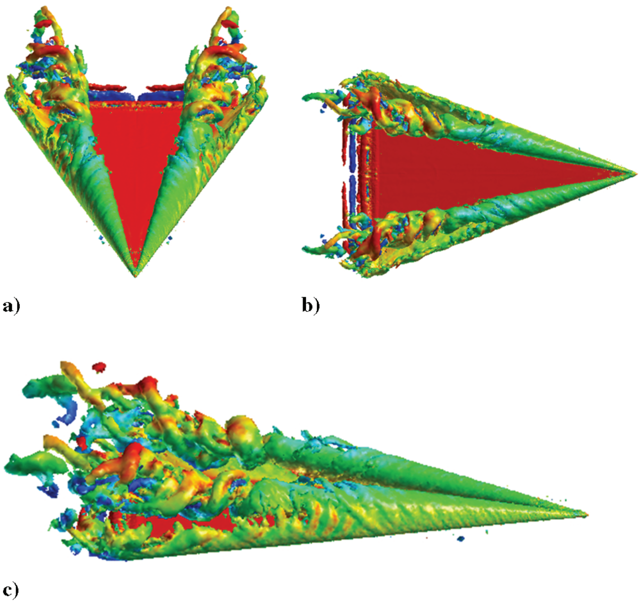

Fig. 5 Instantaneous isosurfaces of vorticity magnitude colored by the spanwise component of vorticity for three views of the 70 deg delta wing G9A4 grid in a freestream (i.e., no wind-tunnel walls and no sting). The flowfield conditions are $\alpha = 27$ deg, $M = 0.069$, and $Re_c = 1.56 \times 10^6$.

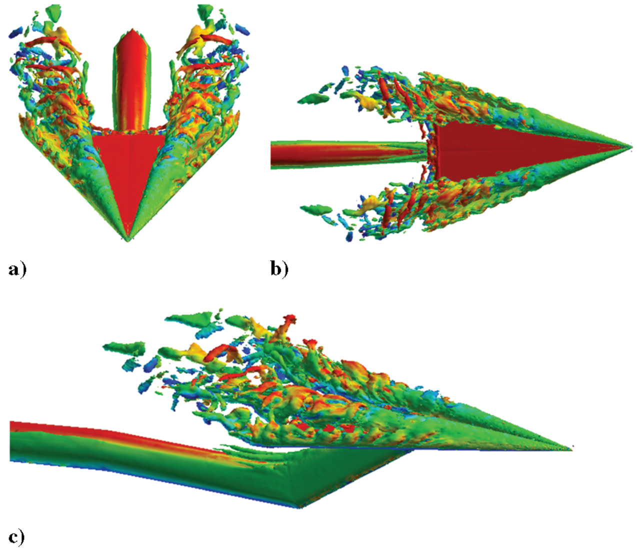

Fig. 6 Instantaneous isosurfaces of vorticity magnitude colored by the spanwise component of vorticity for three views of the 70 deg delta wing G7A1 grid with wind-tunnel walls and a truncated sting modeled. The flowfield conditions are $\alpha = 27$ deg, $M = 0.069$, and $Re_c = 1.56 \times 10^6$.

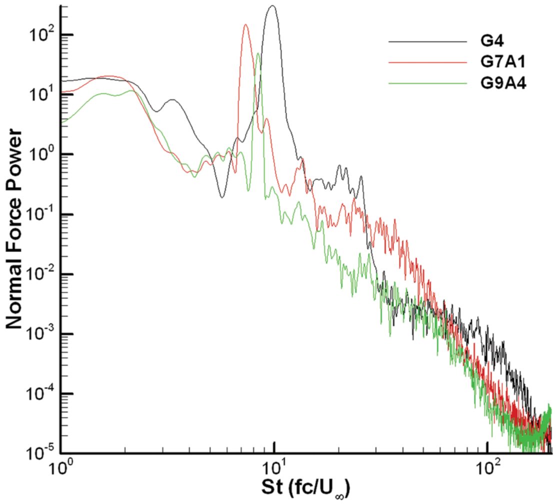

Fig. 7 Power spectral density analysis of the delta wing normal force for three grids. PSD was computed from the last 8000 time steps of a 10,000 time step simulation, and the power is presented with respect to the nondimensional Strouhal frequency. The flowfield conditions are $\alpha = 27$ deg, $M = 0.069$, and $Re_c = 1.56 \times 10^6$.

Turbulence Models

Cobalt has several choices of turbulence models including Spalart–Allmaras (SA) [22] RANS, as well as DES based on SA [14] (called SADES in this work). The SADES hybrid model was found to be a suitable method for the current study by Morton et al. [17] due to the method's ability to eliminate spurious eddy viscosity in the core of vortices and resolve the turbulent scales germain to the delta wing vortex breakdown problem. The following subsections describe the turbulence model used in the current work and also provide references for more detailed descriptions.

Spalart–Allmaras Turbulence Model

The Spalart–Allmaras [22] one-equation turbulence model solves a single partial differential equation for a working variable related to the turbulent viscosity. The differential equation is derived by using empiricism, arguments of dimensional analysis, Galilean invariance, and selected dependence on the molecular viscosity [22]. The model includes a wall destruction term that reduces the turbulent viscosity in the laminar sublayer and the log layer. Details of the model implementation and all coefficients are given in [17].

Detached-Eddy Simulation

The DES model was originally based on the Spalart–Allmaras one-equation RANS turbulence model (discussed previously, with a more detailed presentation in [17]). The wall destruction term is

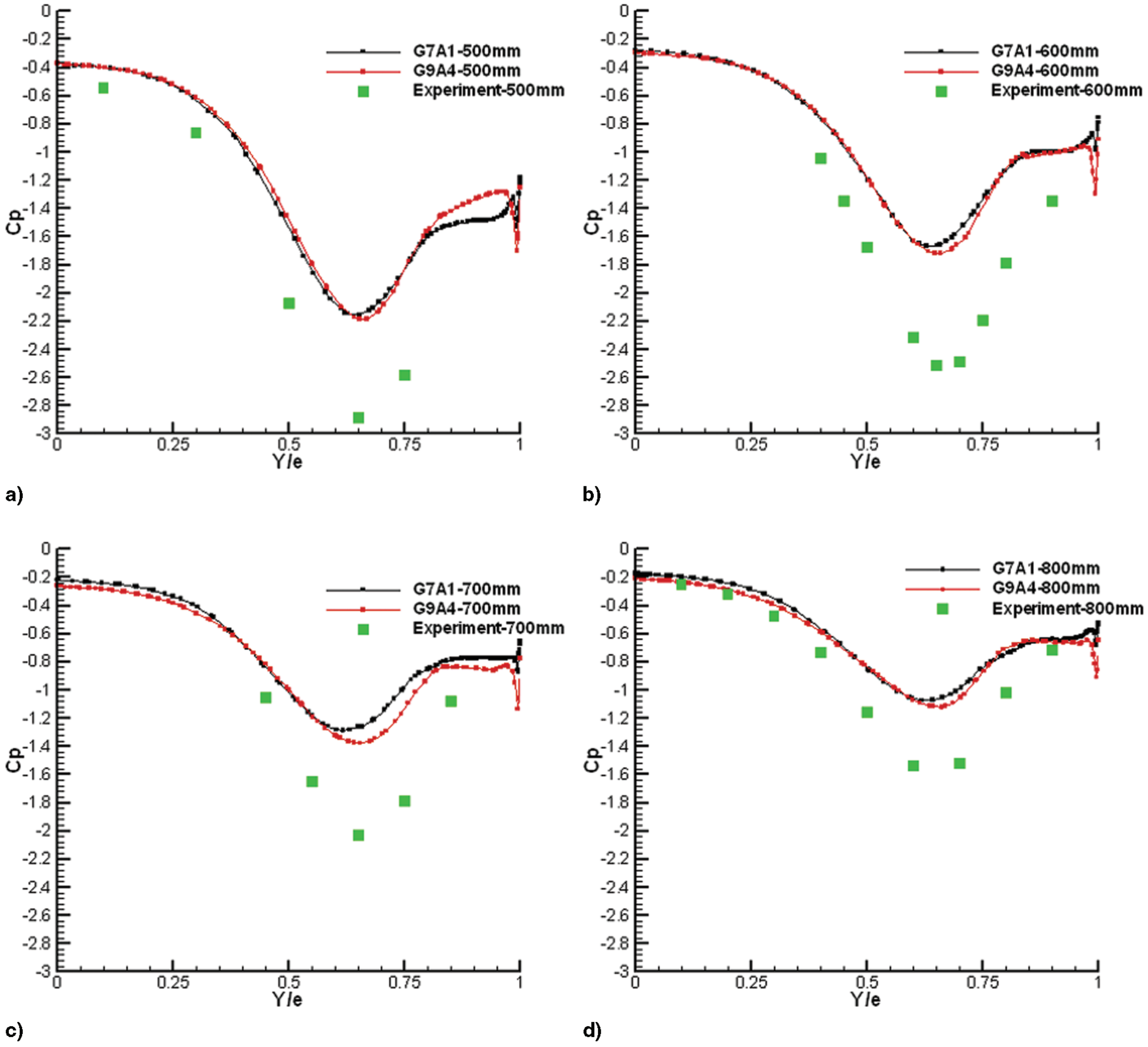

Fig. 8 Average surface pressure coefficients along the span for the G7A1 and G9A4 grid SADES solutions and the experiment at four chordwise stations: a) 500 mm, b) 600 mm, c) 700 mm, and d) 800 mm. The flowfield conditions are $\alpha = 27$ deg, $M = 0.069$, and $Re_c = 1.56 \times 10^6$.

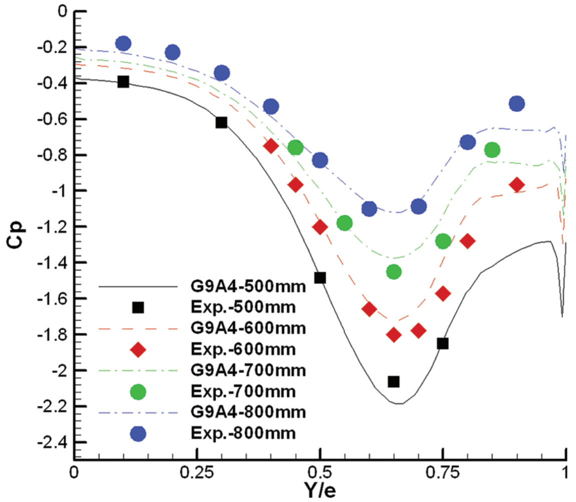

Fig. 9 Average surface pressure coefficients along the span scaled by the square root of 2 for the G9A4 grid SADES solutions and the experiment at four chordwise stations.

proportional to the square of the modified eddy viscosity divided by the distance to the nearest wall $(\tilde{\nu}/d)^2$. When this term is balanced with the production term $\hat{S}$, the eddy viscosity becomes proportional to $\hat{S}d^2$. The Smagorinski LES model varies its subgrid scale turbulent viscosity with the local strain rate, and the grid spacing described by $\nu_{\mathrm{SGS}} \propto \hat{S}\Delta^2$, where $\Delta = \max(\Delta x, \Delta y, \Delta z)$. If d is replaced with Δ in the wall destruction term, the SA model will act as a Smagorinski LES model. To exhibit both RANS and LES behavior, d in the SA model is replaced by

$$\tilde{d} = \min(d, C_{\mathrm{DES}}\Delta), \qquad C_{\mathrm{DES}} = 0.65$$

When $d \ll \Delta$, the model acts in a RANS mode, and when $d \gg \Delta$ the model acts in a Smagorinski LES mode. Therefore, the model switches into LES mode when the grid is locally refined. DES was implemented in an unstructured grid solver by Forsythe et al. [16] They determined the C_{DES} constant could be 0.65, consistent with the structured grid implementation of Shur et al. [23], when the grid spacing Δ was taken to be the longest distance between the cell center and all of the neighboring cell centers. All simulations in this study use the SADES hybrid RANS–LES turbulence model.

Grid Generation

Grids were developed using the software program Gridtool [24] to develop the surface point distributions and background sources and VGRIDns [25] to grow the volume grid. Grids were typically created with concentration of points near the surface in the viscous region and concentration of points in the LES focus region of the vortex core by the use of Gridtool's line sources.

After growing the tetrahedral grid with VGRIDns, a *Cobalt* utility code called *Blacksmith* was used to "weld" the majority of tetrahedra

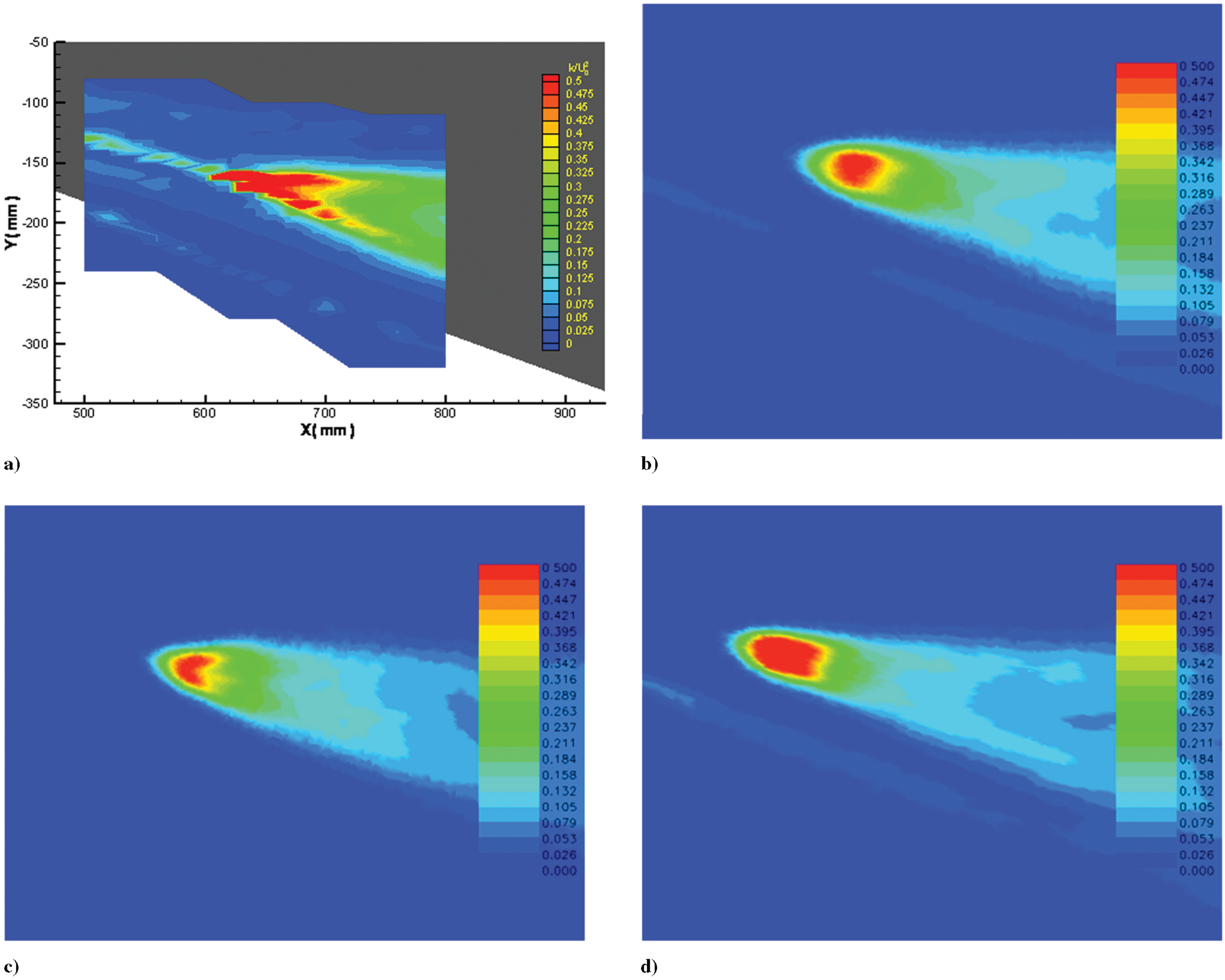

a) b) c) d)

Fig. 10 Experimentally and numerically obtained resolved turbulent kinetic energy nondimensionalized by the freestream velocity squared in a horizontal plane passing through the vortex core: a) ONERA experiments of Mitchell et al. [13], b) G4 SADES solution, c) G9A4 SADES solution, and d) G7A1 SADES solution. The flowfield conditions are $\alpha = 27$ deg, $M = 0.069$, and $Re_c = 1.56 \times 10^6$.

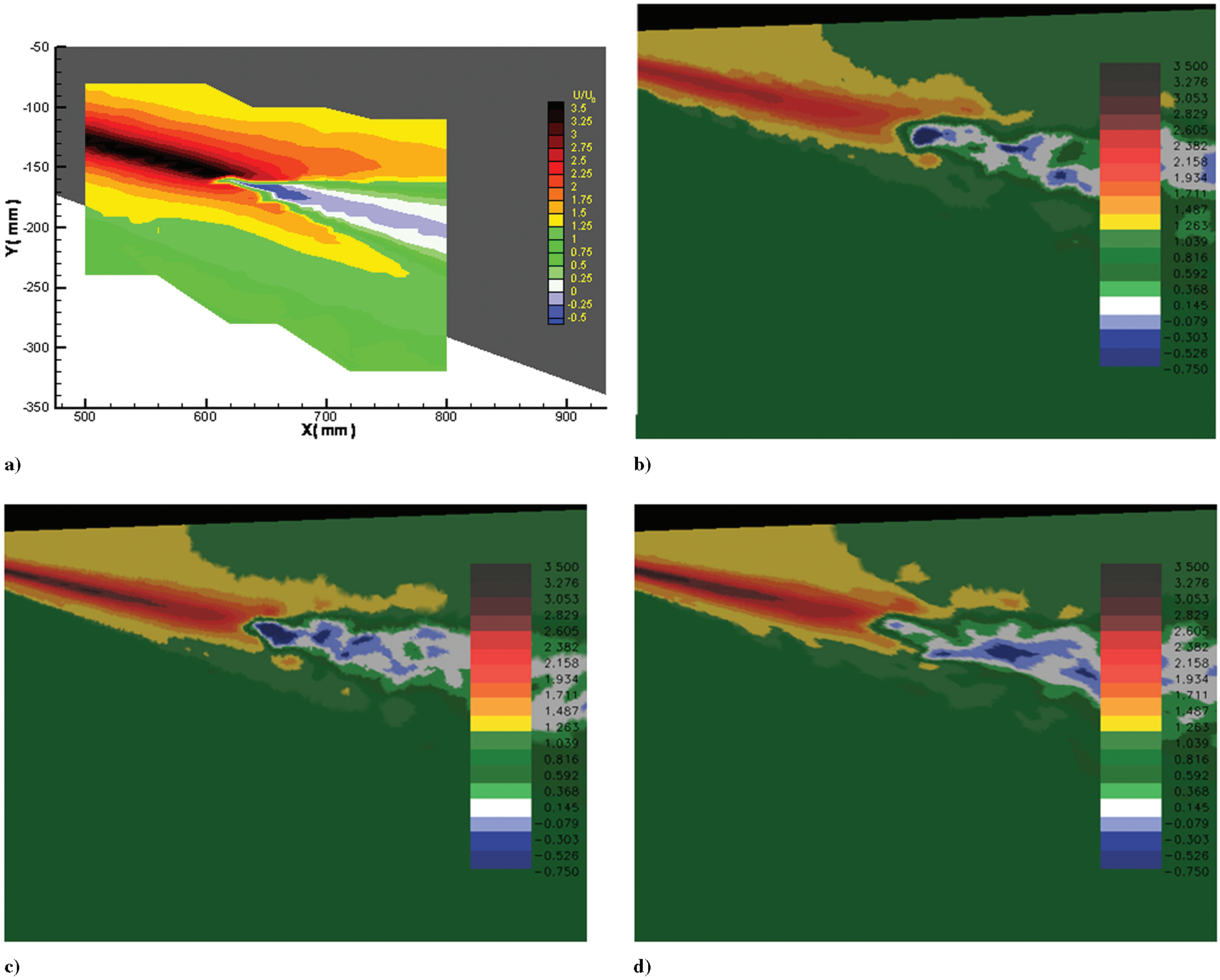

Fig. 11 Experimentally and numerically obtained streamwise velocity component nondimensionalized by the freestream velocity in a horizontal plane passing through the vortex core: a) ONERA experiments of Mitchell et al. [13], b) G4 SADES solution, c) G9A4 SADES solution, and d) G7A1 SADES solution. The flowfield conditions are $\alpha = 27$ deg, $M = 0.069$, and $Re_c = 1.56 \times 10^6$.

in the viscous region into prisms. Using prisms in the viscous region produces a more orthogonal grid by improving the aspect ratio of the cells, and a side benefit is a reduction in the overall number of cells. All of the grids in this study consist of an inner region of over 20 layers with an initial spacing normal to the wall in viscous wall units less than 1, geometric stretching factor of 1.2, and an outer region of nearly isotropic tetrahedra. The inner region consists of at least 13 layers of prisms with the remaining layers tetrahedra. The prism dimensions on the surface were a factor of approximately 200 times larger than the wall normal dimension for all grids.

Grids were also obtained by feature-based adaptive mesh refinement (AMR). This grid technology is particularly well suited for DES because separated flow regions can easily be grid refined. Pirzadeh [26] presented a method based on a tetrahedral unstructured grid technology developed at NASA Langley Research Center with application to two configurations with vortex-dominated flowfields. The large improvement of the adapted solutions in capturing vortex flow structures over the conventional unadapted results was demonstrated by comparisons with wind-tunnel data. Pirzadeh showed that the numerical prediction of these vortical flows was highly sensitive to the local grid resolution, and he also stated that grid adaptation is essential to the application of CFD to these complicated flowfields.

AMR grids were developed with the following procedure: a steady state flow solution was computed for a particular grid, next the flowfield solution was used to create an AMR grid by eliminating all cells within an isosurface of vorticity magnitude at a particular level, and finally the more refined grid was then grown inside of the isosurface by applying a scale factor to the baseline grid density (i.e., 0.5). This procedure was typically performed twice to create a vortex core and shear layer with one-fourth the cell sizes (in all coordinate directions) of the original grid. The new grid was then used to compute unsteady detached-eddy simulations of the flowfield.

There were many grids developed for the current study, including grids with and without wind-tunnel walls, with and without a wind-tunnel sting, full span and half-span, and with and without AMR. Table 1 describes the details of the grids developed for this study. All of the grids were produced with Gridtool and VGRIDns to allow adaptive mesh refinement, if desired.

Computational Results

All simulations of the current study were performed for flowfield conditions of $\alpha = 27$ deg, $M = 0.069$, and $Re_c = 1.56 \times 10^6$. The baseline turbulence treatment is to assume the flow is fully turbulent everywhere and to apply the SADES hybrid model. A study of turbulence treatments for this flowfield was performed and presented in [17]. The study included comparisons of vortex breakdown solutions computed with the Spalart–Allmaras and shear stress transport RANS methods with DES versions of these turbulence models. In addition, the effect of rotation correction for the Spalart–Allmaras model was also described. The study concluded that RANS methods are too dissipative and can eliminate the physically

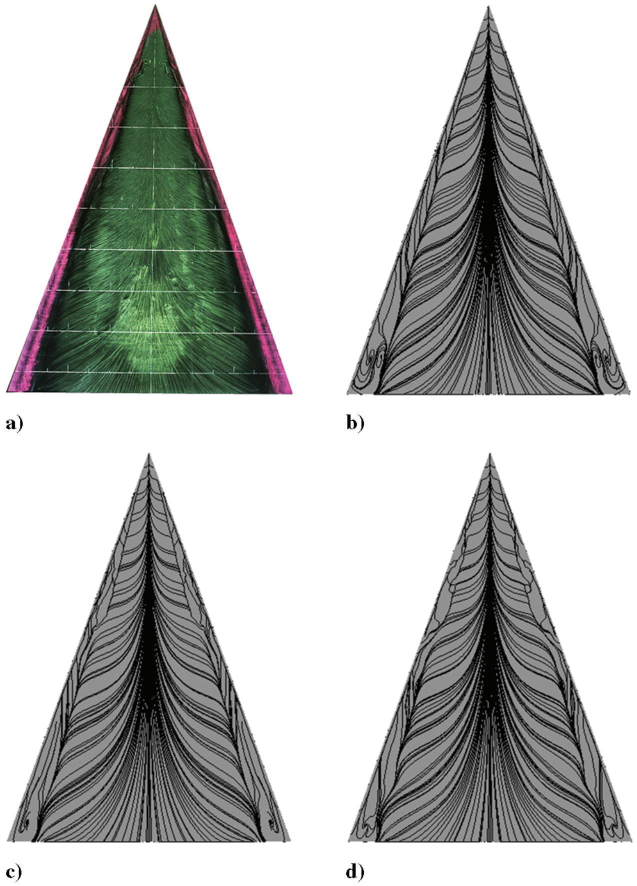

Fig. 12 Surface oil flow patterns: a) experiments of Mitchell et al. [13], b) grid G9A4 fully turbulent, c) grid G9A4 laminar-to-turbulent transition at 30% root chord, and d) grid G9A4 laminar-to-turbulent transition at 40% root chord. The flowfield conditions are $\alpha = 27$ deg, $M = 0.069$, and $Re_c = 1.56 \times 10^6$.

observed vortex breakdown phenomenon, whereas DES is able to capture vortex breakdown accurately.

A systematic time step and Newton subiteration study was presented in [17] for grid G2 (2.7×10^6 cells). The study demonstrated that three Newton subiterations and a time step, nondimensionalized by the freestream velocity and root chord, of 0.0025 was sufficient.

In addition to the time-step study, a consistent grid sensitivity study was performed and presented in [27]. Figure 2 demonstrates the ability of SADES to capture the fine scales of the vortex breakdown phenomena at this high Reynolds number. Instantaneous isosurfaces of vorticity magnitude colored by the spanwise vorticity component are shown for grids G1 (1.2×10^6 cells), G2, (2.7×10^6 cells), G3 (6.7×10^6 cells), and G4 (10.7×10^6 cells).

Typical simulations were run for 10,000 iterations, starting from freestream conditions, and time averages were computed starting after the 2000th iteration to eliminate transients. It is apparent in Figs. 2a–2d that consistent grid refinement provides a significant increase in the number of flowfield structures resolved. In the prebreakdown region of the vortex core, substructures winding around the core are observed as the grid is refined. Also, there is a significant increase in the number of structures observed in the region of the core, postbreakdown, as the grid is refined. Trailing-edge spanwise vortical structures begin to be resolved as the grid is refined, and for grid G4, 3-D structures emanating from the blunt trailing edge that transition to these spanwise coherent vortices are also captured. An instability at the leading edge that is time varying was also captured and resolved with increasing grid density.

The sensitivity of the surface pressure coefficient to grid refinement is depicted in Fig. 3 for four chordwise stations (500, 600, 700, and 800 mm). Although the surface pressure coefficient does vary with grid refinement, grids G3 and G4 are almost indistinguishable from each other. The differences in the surface pressure coefficient are more pronounced aft of breakdown, which occurs at 0.65 (± 0.05) in the experiments.

One of the more difficult quantities to predict is the resolved turbulent kinetic energy (TKE) in the core of the vortex. This quantity is sensitive to the grid density because it is a measure of the production of eddies in the core of the vortex. Figure 4 shows the ability of SADES to capture the resolved TKE and the sensitivity to grid density. The onset of vortex breakdown is signaled by the rapid rise in TKE, and the peak for grid G4 is close to the experimental value of 0.5 (when nondimensionalized by the square of the freestream velocity).

The vortex breakdown position is computed for many of the grids in Table 1 and is presented in Table 2. The definition of vortex breakdown position for the purposes of this study is the chordwise position measured from the apex, where the streamwise velocity goes to zero. The DES solutions are all within the uncertainty band of the experiments, whereas the steady state solution for the G7A1 grid is fairly far forward.

Although the finest grid, G4, was capable of producing relevant solutions for vortex breakdown, the grid cost was high when considering that the aerosurface that produces these vortices on aircraft such as the F-18 is only a small portion of the vehicle. Alleviation of this high cost was attempted with AMR. An AMR grid was produced with2.4×10^6 cells and a concentration of these cells in the vortex core and leading-edge shear layer. Figure 5 depicts three views of the instantaneous solution after 10,000 time steps. This grid is comparable to the G3 grid without AMR composed of 6.7×10^6 cells.

Another AMR grid was produced that incorporated a truncated sting and wind-tunnel walls (Fig. 6). The additional complexity of the sting required a total number of 4.1×10^6 cells. Again, evidence of the leading-edge shear layer instability, trailing-edge vortices, and postbreakdown structures were seen, but in addition, forebody vortices off of the sting are seen as well as interactions of the base shed vortices, and the sting. Grid G7A1 was intended to simulate the ONERA F-2 wind-tunnel walls but the outer boundaries of the grid did not correspond to the test section.

A power spectral density (PSD) analysis was performed for these two grids and compared with the finest grid G4 (Fig. 7) to determine the ability of these grids to capture turbulent structures and also to determine the effect of the sting and wind-tunnel walls on frequency content. The grid G9A4 is lacking in the higher frequency range and is unable to accurately depict the base shedding due to a lack of resolution at the trailing edge. The G7A1 grid, on the other hand, has improved trailing-edge characteristics and also demonstrates some higher frequency content not observed with G4. This additional content is most likely due to sting interactions with the delta wing structures and/or shedding off of the sting itself. It is interesting to note the sting forebody vortices that are visible in the "elbow" (see Fig. 6c).

Figure 8 depicts the surface pressure coefficient versus span at four chordwise positions for the G7A1 and G9A4 grids, as well as the experiments of Mitchell et al. [13]. Minor differences are seen between the G7A1 and G9A4 grids primarily in the postbreakdown locations 700 and 800 mm. This figure does, however, point out the major discrepancy with the experiments is observed for all grids for the coefficient of pressure, or Cp, on the surface. For example, the experimental peak Cp at $X = 500$ mm is -2.9, whereas the G7A1 and G9A4 grids give a value of -2.2 (a difference of 24%). This difference is typical of all of the surface Cp data for all of the grids computed. In addition, it should be noted that all of the other researchers participating in this international CFD experimental comparison obtained similar results. Goertz [28] computed solutions of the same configuration and flowfield conditions using a structured Navier–Stokes multiblock code (NSMB) with a detached-eddy simulation turbulence treatment. His comparison of the peak difference at 500 mm was 23.8%. Soewarmoto and Moelens [29] computed solutions using a structured Navier–Stokes solver with a RANS turbulence treatment, and their peak difference at 500 mm

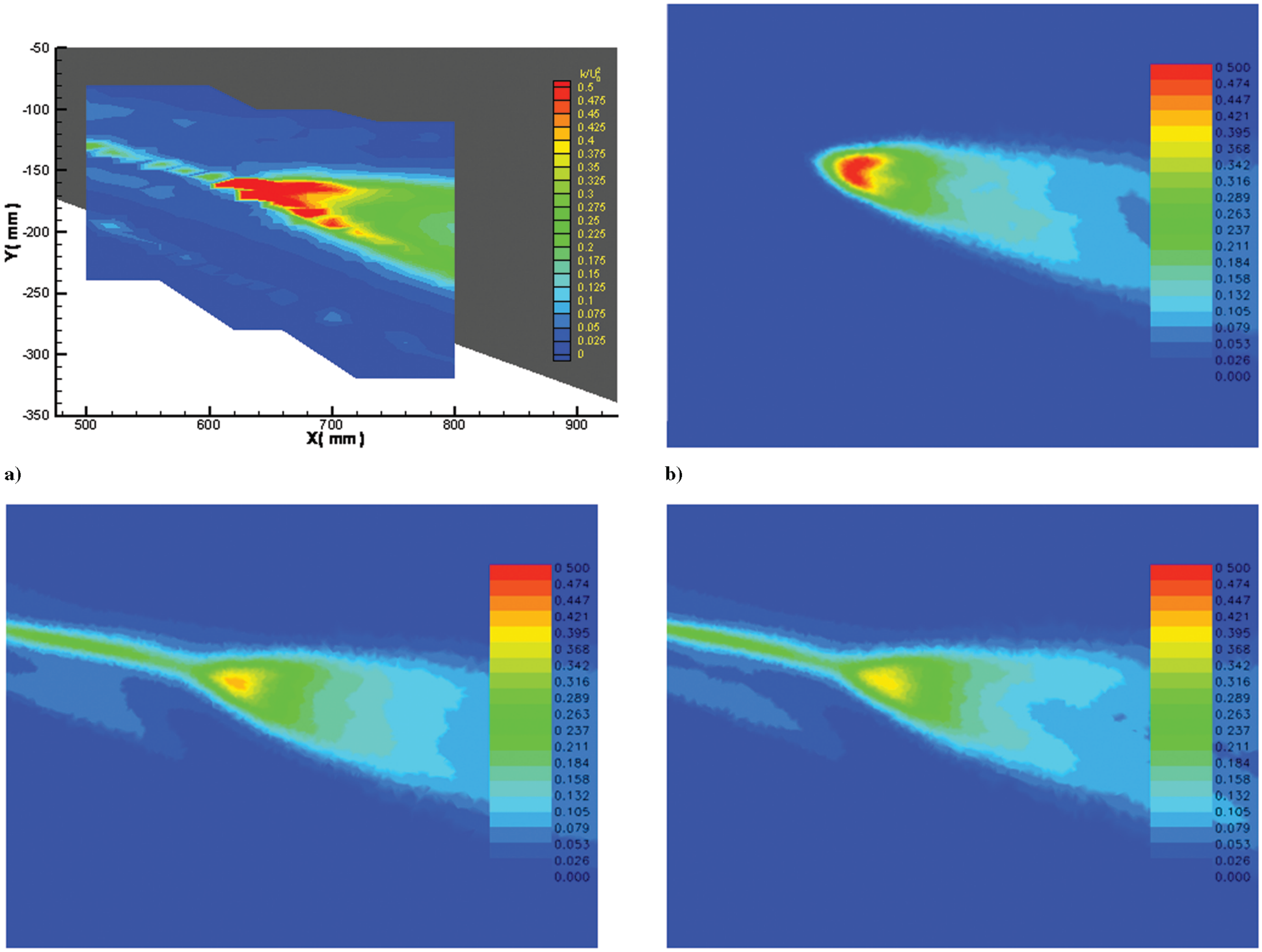

a)

b)

c)

d)

Fig. 13 Experimentally and numerically obtained resolved turbulent kinetic energy nondimensionalized by the freestream velocity squared in a horizontal plane passing through the vortex core: a) ONERA experiments of Mitchell et al. [13], b) grid G9A4 fully turbulent, c) grid G9A4 laminar-to-turbulent transition at 30% root chord, and d) grid G9A4 laminar-to-turbulent transition at 40% root chord. All solutions were computed using SADES and for flowfield conditions of $\alpha = 27$ deg, $M = 0.069$, and $Re_c = 1.56 \times 10^6$.

was 22.4%. LeRoy et al. [30] used the Navier–Stokes solver FLUENT and a RANS turbulence treatment, and his peak difference at 500 mm was also 23.8%. So several researchers using several computational codes obtained essentially the same surface Cp results for this flowfield.

In an effort to determine whether the experimental and computational results were scaled differently, the current results were scaled until the 500 mm chordwise station matched, and then the other stations were examined to determine the quality of the comparison. Figure 9 depicts the solution of the G9A4 grid for chordwise stations 500, 600, 700, and 800 mm scaled by the square root of 2. As one can see, the comparison of all stations is impressive. The author can only speculate that a possible source of the difference between all of the computational simulations and the experimental results for surface Cp could be due to a difference in the reference dynamic pressure scaling. It should be noted that an exhaustive grid sensitivity, time step sensitivity, wind-tunnel wall sensitivity, angle-of-attack sensitivity, and laminar-to-turbulent transition sensitivity on surface Cp was accomplished with only a few percent variation.

The turbulent kinetic energy in a plane parallel to the delta wing surface through the vortex core was also analyzed (Fig. 10). All three of the grids, G4, G7A1, and G9A4, produce TKE of the same magnitude as the experiment in the correct region of the flow post-breakdown. It is interesting to note that none of the grids reproduce the TKE generated in the core of the vortex prebreakdown.

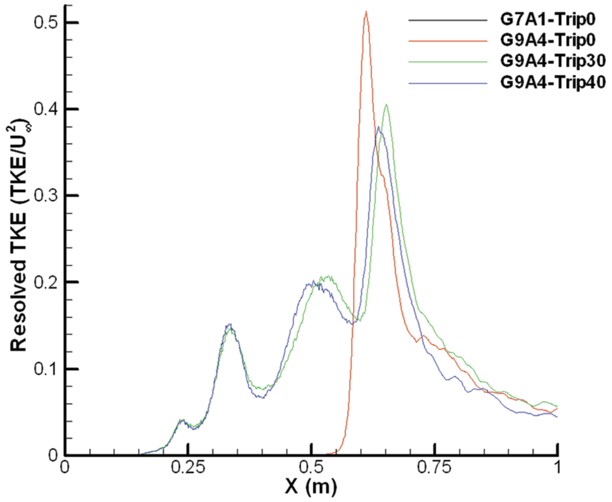

Fig. 14 Resolved turbulent kinetic energy nondimensionalized by the freestream velocity squared along the core of the vortex for the G9A4 grid with a fully turbulent assumption, an assumed laminar-to-turbulent transition at 30% root chord, and laminar-to-turbulent transition at 40% root chord. The flowfield conditions are $\alpha = 27$ deg, $M = 0.069$, and $Re_c = 1.56 \times 10^6$.

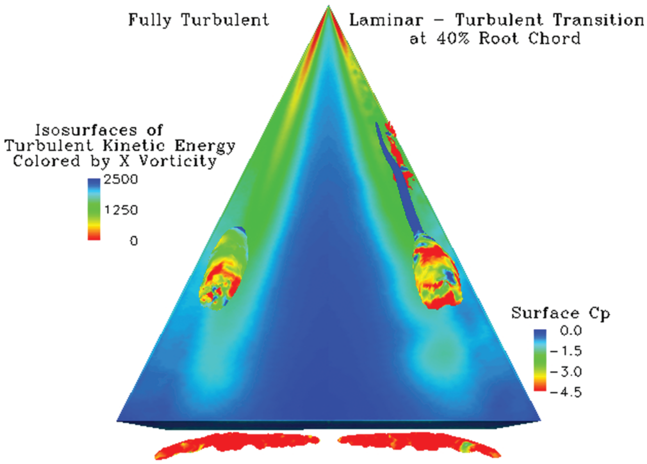

Fig. 15 Isosurfaces of turbulent kinetic energy for the 70 deg delta wing. Left half depicts the SADES fully turbulent solution and the right half depicts the SADES solution with a laminar-to-turbulent transition at 40% root chord. The delta wing surface is colored by the surface pressure coefficient. The flowfield conditions are $\alpha = 27$ deg, $M = 0.069$, and $Re_c = 1.56 \times 10^6$.

Figure 11 depicts the comparison of the streamwise component of local velocity (nondimensionalized by the freestream velocity) with the experiments in a plane horizontal to the delta wing surface through the core of the vortex. Both AMR grids, G7A1 and G9A4, are similar to the experimental data, but the core streamwise component of velocity is slightly lower for the unadapted G4 grid.

All of the previous solutions have been for fully turbulent flow on the leeward and windward sides of the delta wing. Mitchell et al. [13] have suggested that there is a transition from laminar-to-turbulent flow on the leeward side of the delta wing at approximately 40% of the root chord based on oil flow visualization (see Fig. 12a). In an effort to determine the effect of laminar-to-turbulent flow transition, simulations were conducted for an assumed fully turbulent solution, an assumed laminar-to-turbulent transition at 30% root chord, and an assumed transition at 40% root chord. In both cases in which transition was simulated, the windward side was assumed to be laminar. This was implemented by zeroing the production of eddy viscosity in a specified region of the flow (i.e., forward of 40% above the wing and all of the lower wing). Figure 12a depicts the experimental oil flow visualization in which a "pinching" of the secondary separation line occurs at the 40% root chord station. The fully turbulent SADES solution shown in Fig. 12b gives a straight secondary separation line from the apex to the trailing edge. The laminar-to-turbulent transition SADES solutions, on the other hand, do manifest the pinching of the secondary separation line, and the 40% solution compares very favorably to the experiment.

The resolved TKE in a plane parallel to the delta wing surface through the vortex core shows the effect of the laminar flow upstream of breakdown (Fig. 13). The fully turbulent solution of Fig. 13b exhibits no TKE in the core upstream of breakdown, whereas the 30 and 40% transition solutions of Fig. 13c and 13d, respectively, compare very well to the experiment. The peak magnitude of the TKE is lower, but the grid sensitivity study discussed previously shows the sensitivity of the peak TKE to grid density, indicating the possible need for more points in the core.

Figure 14 depicts the TKE along the core of the vortex for fully turbulent flow and transitions at 30 and 40% root chord. The fully turbulent solution generates turbulent kinetic energy in the vortex core starting at breakdown. The transitional solutions both generate turbulent kinetic energy well upstream of the forced transition in the boundary layer of 30 or 40%. The peaks and valleys of the transitional solutions upstream of breakdown are due to the fact that the core is no longer straight, and the line plot of TKE is moving in and out of the center of the core (see Fig. 15).

Figure 15 depicts the contrast between the fully turbulent solution (left side) and the 40% transition solution (right side). The core of the primary vortex and the secondary vortex both generate turbulent kinetic energy upstream of breakdown, whereas the fully turbulent solution does not. Also, the curved nature of the vortex core is evident.

Conclusions

Spalart–Allmaras detached-eddy simulations of a delta wing experiencing vortex breakdown were successfully computed and compared with very detailed experiments. These solutions were shown to be sensitive to grid density and were greatly improved with adaptive mesh refinement. In fact, two grids were shown to give essentially the same solution, even though the AMR grid has half of the standard grid points.

The effect of more detailed geometry of the test, such as a truncated sting mount and the wind-tunnel walls, was also assessed. The effect of the sting is to add frequency content in the higher frequency range and also to interact with the delta wing trailing vortices. The effect of wind-tunnel walls was not successfully assessed because the actual ONERA F2 tunnel geometry was not accurately modeled with the grids. The G7A1 grid is much larger in the test section than the ONERA F2 tunnel. Assessment of the actual wind-tunnel wall geometry is suggested as a future area of research.

One of the most striking findings of this effort is the importance of modeling the laminar-to-turbulent transition. This is routinely assumed to have little effect or is determined to be too difficult to implement due to a lack of good transition models. Unfortunately, for this flowfield, it has a measurable effect on turbulent kinetic energy and the surface oil flows.

Acknowledgments

The author would like to express appreciation to Shahyar Pirzadeh for his help producing adaptively refined meshes as well as his enlightening discussions during this work, and Russ Cummings for his help in preparing the manuscript. The author would also like to thank the U.S. Air Force Office of Scientific Research for funding this project under the direction of John Schmisseur, and the Aeronautical Systems Center and Maui High Performance Computing Centers for their generous support of computational hours.

References

[1] Lovell, D. A., "Military Vortices," *Symposium on Advanced Flow Management Part A - Vortex Flows and High Angle of Attack for Military Vehicles*, RTO-MP-069(I), NATO Research and Technology Organisation, 2001.

[2] Werlé, H., "Quelques Résultats Expérimentaux sur les Ailes en Flèche, aux Faibles Vitesses, Obtenus en Tunnel Hydrodynamique," *La Recherche Aéronautique*, Vol. 41, Sept.–Oct. 1954, pp. 15–21.

[3] Peckham, D. H., and Atkinson, S. A., "Preliminary Results of Low Speed Wind Tunnel Tests on a Gothic Wing of Aspect Ration 1.0," CP-508, Aeronautical Research Council, April 1957.

[4] Elle, B. J., "An Investigation at Low Speed of the Flow near the Apex of Thin Delta Wings with Sharp Leading Edges," Aeronautical Research Council, Reports and Memoranda No. 3176, 1961.

[5] Lambourne, N. C., and Bryer, D. W., "The Bursting of Leading-Edge Vortices: Some Observations and Discussion of the Phenomenon," Aeronautical Research Council, R&M No. 3282, 1962.

[6] Hall, M. G., "Vortex Breakdown," *Annual Review of Fluid Mechanics*, Vol. 4, 1972, pp. 195–218.
doi:10.1146/annurev.fl.04.010172.001211

[7] Leibovich, S., "The Structure of Vortex Breakdown," *Annual Review of Fluid Mechanics*, Vol. 10, 1978, pp. 221-246.
doi:10.1146/annurev.fl.10.010178.001253

[8] Sarpkaya, T., "On Stationary and Traveling Vortex Breakdowns," *Journal of Fluid Mechanics*, Vol. 45, Pt. 3, 1971, pp. 545–559.
doi:10.1017/S0022112071000181

[9] Nelson, R. C., "Unsteady Aerodynamics of Slender Wings," *Aircraft Dynamics at High Angles of Attack: Experiments and Modeling*, AGARD Rept. 776, 1991, pp. 1-1–1-26.

[10] Délery, J., "Aspects of Vortex Breakdown," *Progress in Aerospace Sciences*, Vol. 30, 1994, pp. 1–59.
doi:10.1016/0376-0421(94)90002-7

[11] Faller, J. H., and Leibovich, S., "Disrupted States of Vortex Flow and

Vortex Breakdown," *Physics of Fluids*, Vol. 20, No. 9, 1977, pp. 1385–1400.
doi:10.1063/1.862033

[12] Menke, M., Yang, H., and Gursul, I., "Further Experiments on Fluctuations of Vortex Breakdown Location," AIAA Paper 96-0205, Jan. 1996.

[13] Mitchell, A. M., Molton, P., Barberis, D., and Délery, J., "Oscillation of Vortex Breakdown Location and Control of the Time-Averaged Location by Blowing," *AIAA Journal*, Vol. 38, No. 5, May 2000, pp. 793–803.

[14] Spalart, P. R., Jou, W.-H., Strelets, M., and Allmaras, S. R., "Comments on the Feasibility of LES for Wings, and on a Hybrid RANS/LES Approach," *Advances in DNS/LES, 1st Air Force Office of Scientific Research International Conference on DNS/LES*, Greyden Press, Columbus, OH, Aug. 1997.

[15] Strang, W. Z., Tomaro, R. F., and Grismer, M. J., "The Defining Methods of *Cobalt*: A Parallel, Implicit, Unstructured Euler/Navier-Stokes Flow Solver," AIAA Paper 99-0786, Jan. 1999.

[16] Forsythe, J. R., Hoffmann, K. A., Cummings, R. M., and Squires, K. D., "Detached-Eddy Simulation with Compressibility Corrections Applied to a Supersonic Axisymmetric Base," *Journal of Fluids Engineering*, Vol. 124, No. 4, 2002, pp. 911–923.
doi:10.1115/1.1517572

[17] Morton, S. A., Forsythe, J. R., Mitchell, A. M., and Hajek, D., "Detached-Eddy Simulations and Reynolds-Averaged Navier-Stokes Simulations of Delta Wing Vortical Flowfields," *Journal of Fluids Engineering*, Vol. 124, No. 4, 2002, pp. 924–932.
doi:10.1115/1.1517570

[18] Squires, K. D., Forsythe, J. R., and Spalart, P. R., "Detached-Eddy Simulation of the Separated Flow Around a Fore Body Cross-Section," *Direct and Large Eddy Simulation IV*, ERCOFTAC Series, edited by B. J. Geurts, R. Friedrich, and O. Metais, Vol. 8, Kluwer Academic, Norwell, MA, 2001, pp. 481–500.

[19] Forsythe, J. R., Squires, K. D., Wurtzler, K. E., and Spalart, P. R., "Detached-Eddy Simulation of Fighter Aircraft at High Alpha," AIAA Paper 2002-0591, Jan. 2002.

[20] Forsythe, J. R., and Woodson, S. H., "Unsteady CFD Calculations of Abrupt Wing Stall Using Detached-Eddy Simulation," AIAA 2003-0594, Jan. 2003.

[21] Mitchell, A. M., and Molton, P., "Vortical Substructures in the Shear Layers Forming Leading-Edge Vortices," AIAA Paper 2001-2424, June 2001.

[22] Spalart, P. R., and Allmaras, S. R., "A One Equation Turbulence Model for Aerodynamic Flows," *La Recherche Aerospatiale: Bulletin Bimestriel de l'Office National d'Etudes et de Recherches Aerospatiales*, Vol. 1, No. 1, 1994, pp. 5–21.

[23] Shur, M., Spalart, P. R., Strelets, M., and Travin, A., "Detached Eddy Simulation of an Airfoil at High Angle of Attack," *4th International Symposium of Engineering Turbulence Modelling and Measurements*, Elsevier, Amsterdam, 1999, pp. 669–678.

[24] Samareh, J., "Gridtool: A Surface Modeling and Grid Generation Tool," *Proceedings of the Workshop on Surface Modeling, Grid Generation, and Related Issues in CFD Solution*, NASA CP-3291, May 1995.

[25] Pirzadeh, S., "Progress Toward a User-Oriented Unstructured Viscous Grid Generator," AIAA Paper 96-0031, Jan. 1996.

[26] Pirzadeh, S., "Vortical Flow Prediction Using an Adaptive Unstructured Grid Method," *Symposium on Advanced Flow Management Part A - Vortex Flows and High Angle of Attack for Military Vehicles*, RTO-MP-069(I), NATO Research and Technology Organisation2001.

[27] Morton, S. A., Forsythe, J. R., Squires, K. D., and Wurtzler, K. E., "Assessment of Unstructured Grids for Detached-Eddy Simulation of High Reynolds Number Separated Flows," *8th International Society of Grid Generation Conference*, International Society of Grid Generation, 2003.

[28] Goertz, S., "Detached-Eddy Simulations of a Full-Span Delta Wing at High Incidence," AIAA Paper 2003-4216, 2003.

[29] Soewarmoto, B. I., and Boelens, O. J., "Simulation of Vortical Flow Over a Slender Delta Wing Experiencing Vortex Breakdown," AIAA Paper 2003-3942, 2003.

[30] LeRoy, J. F., Mary, I., and Rodriguez, O., "CFD Solutions of 70-deg Delta Wing Flows," AIAA Paper 2003-4219, 2003.